Article

Planar Hot-Electron Photodetection with Tamm Plasmons

Cheng Zhang, Kai Wu, Vincenzo Giannini, and Xiaofeng Li

ACS Nano, **Just Accepted Manuscript** • DOI: 10.1021/acsnano.6b07578 • Publication Date (Web): 24 Jan 2017

ACS Nano is published by the American Chemical Society. 1155 Sixteenth Street N.W., Washington, DC 20036

Planar Hot-Electron Photodetection with Tamm Plasmons

Cheng Zhang,[a,b] Kai Wu,[a,b] Vincenzo Giannini,[c] and Xiaofeng Li[a,b,*]

[a]*College of Physics, Optoelectronics and Energy & Collaborative Innovation Center of Suzhou Nano Science and Technology, Soochow University, Suzhou 215006, China;*
[b]*Key Lab of Advanced Optical Manufacturing Technologies of Jiangsu Province & Key Lab of Modern Optical Technologies of Education Ministry of China, Soochow University, Suzhou 215006, China;*
[c]*Blackett Laboratory, Imperial College London, Prince Consort Road, London SW7 2BZ, United Kingdom.*
*E-mail: *xfli@suda.edu.cn*

ABSTRACT. There is an increasing interest in harvesting the photoejected hot-electrons for sensitive photodetectors, which have highly tunable detection wavelengths controlled by structural engineering rather than the classic doped semiconductors. However, the widely employed metallic nanostructures which excite surface plasmons (SPs) to enhance the photoemission of hot-electrons are usually complex with a high fabrication challenge. Here we present a purely planar hot-electron photodetector based on Tamm plasmons (TPs), by introducing distributed Bragg reflector integrated with hot-electron collection layers in metal/semiconductor/metal configuration. Results show that the light incidence can be strongly confined in the localized region between the top metal and the adjacent dielectric layer due to the excitation of TP resonance, so that more than 87% of the light incidence can be absorbed by the top metal layer. This enables a strong and unidirectional photocurrent and a photoresponsivity which can even be higher than that of the conventional nanostructured system. Moreover, the planar TP system shows a narrow-band resonance with a high tunability, a good resistance against the change of the incident angle, and the possibility for extended functionalities. The proposed TP-based planar configuration significantly simplifies the conventional SP-based systems and opens up the pathway for high-performance low-cost hot-electron photodetection.

KEY WORDS: Tamm plasmons; surface plasmons; hot electrons; photodetector; photoresponsivity

The energetic hot electrons excited through photon absorption in metals can be extracted *via* internal photoemission for a number of applications, *e.g.*, photodetection,[1–5] photovoltaics,[6,7] photocatalysis,[8,9] and surface imaging.[10,11] In terms of photodetection, the hot-electron mechanism enables the direct and efficient below-bandgap photodetection, the high tunability of the working wavelength through manipulating the structured resonance instead of the materials, and the possibility of room-temperature operation.[12,13] Indeed, direct illumination on a metal film can excite hot electrons, but with an extremely low efficiency due to the lack of effective light-trapping mechanisms.[14,15] Surface plasmons (SPs) provide an interesting solution since they can strongly localize the photon energy within a deep-subwavelength region, where extensive hot electrons can be generated.[16–20] Nevertheless, almost all of the existing SPs-based hot-electron devices employ the metal/dielectric hybrid systems with delicately designed nanostructures,[21–27] which normally have the in-plane subwavelength (or deep-subwavelength) patterns and require complicated/costly fabrications.[23] Therefore, part of the attention goes back to the planar scenarios for cost-effective strategies. Unfortunately, planar systems are normally not good at trapping light unless the one-dimensional multi-layer system has been carefully designed. For example, it was demonstrated that by integrating the metal/semiconductor/TCO junction (TCO: transparent conductive oxide) into an asymmetric microcavity, the optical absorption in metal can be substantially enhanced.[28] However, the micro-cavity system needs two distributed Bragg reflectors (DBRs), leading to a relatively thick device, which also brings a challenge to the fabrication.

Recently, a type of SPs named as the Tamm plasmons (TPs), which are also called as the optical Tamm states, formed at the boundary between a metal and a DBR was predicted and demonstrated.[29–31] By TPs, the electromagnetic surface wave propagating along the metal/DBR interface can be highly confined in the region around the metal/dielectric interface, allowing a strong absorption by the metal layer.[32] In contrast to SPs, with the assistance of the DBR, TPs in planar systems can be efficiently excited from free space without any polarization discriminations and thus can find very broad applications,[33] including photovoltaics,[34] sensors,[35–37] polariton lasers,[38] detectors[39] and optical switches.[40] Here, we report a TP-based hot-electron photodetector (TP-HE PD), where a properly engineered DBR is integrated with the metal/semiconductor/metal (MSM) hot-electron layers. With the strong coupling of the band-engineered DBR and the MSM HE-cavity, an intensive TP resonance can be excited with a high tunability in a broad spectral range and a good tolerance against the variation of the incident angle. Electromagnetic simulation predicts a near-unity optical absorption at the TP resonance and more than 87% absorption by the top metal layer, allowing a strongly asymmetric optical absorption for a high unidirectional photocurrent. Moreover, the purely planar and thin metallic design facilitates the hot-electron transport in the device, so that a high photoresponsivity, which is over 2 times of that based on the conventional grating-coupled SP-HE PD system, can be achieved. We believe that the planar hot-electron photodetection system based on the excitation of TPs could be a promising candidate for low-cost and sensitive hot-electron photodetection applications.

We first have a brief review on Tamm plasmons excited from the special planar systems. TPs are tightly confined electromagnetic states at the boundary between a metal and a DBR, in analogy with electron states predicted by Tamm in condensed matters.[29] In contrast to the conventional SPs, the wave vector of TPs lies inside the light cone given by $k = \omega/c$, where k is the in-plane wave vector and ω is the angular frequency. Therefore, TPs can be optically excited from free space under any polarizations without needing the vector-matching treatments by gratings, nanoparticles or prisms. To illustrate how the electromagnetic field is confined by TPs, we consider the planar multilayer structure comprising a front DBR and a semi-infinite Au layer as shown in the inset of Figure 1a. The DBR consists of 8 pairs of alternating Al_2O_3/TiO_2 layers ($N_{DBR} = 8$), each layer with a quarter-wavelength optical thickness, and the DBR central wavelength λ_{DBR} is 750 nm. Figure 1a shows the vertical (along z) profile of the normalized electric field $|E|^2$ for the TP resonance. It is found that the strongest electric field occurs at the location very close to the M/DBR interface. Figure 1b plots the reflection spectra of the bare DBR and the DBR+M structure. It is clear that there exists a narrow reflection dip in the forbidden band of DBR by using the DBR+M structure, which indicates the excitation of TPs.

RESULTS AND DISCUSSION

Figure 1c shows the schematic of the proposed TP-HE PD under the planar configuration, which is composed of the silica substrate, MSM stack, and DBR. Here M+DBR is used to excite the TP in the M/DBR interface[29–31] and MSM is used to collect the generated hot electrons.[27,28] Unless specific indication, the thicknesses of the top metal (Au), intermediate semiconductor (ZnO), and bottom metal (Au) layers are 25, 5, and 200 nm, respectively; the DBR pair number (N_{DBR}), DBR central wavelength (λ_{DBR}), and layer thicknesses of DBR are inherited from Figure 1a. Being different from the conventional metal/semiconductor devices based on Schottky junctions, the semiconductor used here is intrinsic; therefore, it is just a modified MIM (I: insulator) system under the same operation principle.[13] The employment of the wide-bandgap (3.3 eV)[41] semiconductor (ZnO) leads to a decreased barrier height [Φ_B ~ 0.9 eV, *i.e.*, the difference between the work function W (5.1 eV)[42] of Au and the electron affinity χ (4.2 eV)[43] of ZnO], which allows the hot-electron photodetection into the infrared range as well as facilitates the hot electron transport through the barrier. Moreover, Figure 1c shows that the special design of MSM+DBR allows an extremely low reflection dip by the device (device transmittance is zero with the presence of the rear Au reflector), affirming a greatly strengthened TP. It is noticed that the thickness of the top Au layer (*i.e.*, adjacent to the DBR) is much smaller than the mean free path (MFP) of electrons in Au (~ 40 nm for low-energy electrons)[44] to ensure a high probability for the generated hot electrons to reach the M/S interface before thermalization and finally accomplish the interfacial electron transfer process.[15] Besides, it is crucial that TiO_2 (*i.e.*, the high-index layer) has to be the layer adjacent to the MSM to ensure the excitation of TPs.[29] For discussion convenience, the thicknesses of the bottom TiO_2 layer and top Au layer are defined as d_{TiO_2} and d_{Au}, respectively.

Hot electrons are generated through the non-radiative decay of plasmon resonances, thermalized by electron-electron scattering in tens of femtoseconds (10–100 fs) after excitation, and subsequently cooled down *via* energy transfer to the lattice by electron-phonon scattering picoseconds later (100 fs to 1ps). Ultimately, the lattice phonons come to equilibrium with the surroundings of the metallic structure on the 100 ps timescale.[7,19] The performance of the TP-HE PD can be determined by considering the following consecutive processes as depicted by the energy band diagram shown in Figure 1d.[13] Upon generation *via* illumination and TP resonances, half of the generated hot electrons will diffuse towards the M/S interface, but only a fraction of them will reach the interface without losing energy in an inelastic collision. Moreover, the generated hot electrons by the top Au layer must propagate across the ultra-thin intermediate ZnO layer and finally be collected by the opposite contact. To get the device photocurrent, we need to calculate the probability of the generated hot electrons to be injected into the semiconductor, propagate across the semiconductor, and be collected by the opposite electrode. For the MSM system, there are two counter-propagating electron flows from both electrodes so that the net photocurrent determines the overall performance of the system. This condition requires a strongly asymmetric absorption in the top and bottom Au layers.[25] In the following discussion, the detailed optical and electrical performances will be studied.

Before the electrical evaluation of the TP-HE PD, the optical performance (light-trapping capability) has to be examined. Based on the optical constants from Palik,[45] rigorous coupled-wave analysis (RCWA) is first employed to study the optical dispersion characteristics in order to properly configure the device for the excitation of TP resonance.[46] The reasons to use RCWA are as follows: 1) it is computationally efficient for a large range of parametrical optimization and 2) it is readily to be extended for nanostructured systems (*e.g.*, multi-layered grating systems) in the future. The detailed optical response including the electric field distribution and the optical absorption by each layer is analyzed by solving Maxwell's equations *via* the finite-element method (FEM).[47] Following the same procedures, when introducing other materials, the measured frequency-dependent dielectric constant can be used in RCWA and FEM. Taking into account the resistive loss ($P_{\text{resistive}}$ ~30%) of the absorbed energy, which is dissipated without hot electrons generation due to the intrinsic lifetime of the electronic states comprising the collective oscillation,[44] the spatially dependent hot-electron generation rate (G) can be written as:

$$G(x,z,\omega) = (1 - P_{resistive})\varepsilon_i |E(x,z,\omega)|^2/(2\hbar) \qquad (1)$$

where ω is the angular frequency, ε_i the imaginary part of the material permittivity, $E(x, y, z)$ the electric field at position (x, y, z), and $\hbar$ the reduced Planck constant. The calculations of the absorption efficiency (A) and detailed derivation of hot-electron generation rate can refer to Section 1 of the *Supporting Information*.[48]

With confirming the excitation of strong TP by the DBR+MSM as shown in Figure 1c, we now investigate 1) how to obtain the strongest TP by properly controlling the number of DBR pairs [N_{DBR}, Figure 2a and 2c] and 2) how to tune the resonance by engineering the thickness of the bottom TiO_2 layer [d_{TiO_2}, Figure 2b] or the central wavelength of DBR [λ_{DBR}, Figure 2d]. Figure 2a exhibits a dark reflection spot (indicating the excitation of TPs) appearing in the optical forbidden band of the DBR. Moreover, it is revealed that the parameter N_{DBR} has a strong impact on the reflection characteristic of the device. When the DBR layers are too few, most of light is reflected back due to the high reflectance of the rear Au reflector; however, with a large N_{DBR}, most of light is reflected directly by DBR without entering the system. Therefore, a proper N_{DBR} is crucial for the realization of a strong TP. These can be easily seen from Figure 2c which plots the device reflection at the TP wavelength (*i.e.*, λ_{TP} = 813 nm) as a function of N_{DBR}, where the reflection of a bare DBR at the same wavelength is shown for reference. A deeper analysis regarding the effect of N_{DBR} and the field confinement of TPs in the proposed TP-HE PD can be found in Section 2 of the *Supporting Information*.

On the other hand, the tunability of TP resonance can be realized by adjusting d_{TiO_2} (Figure 2b) or λ_{DBR} (Figure 2d). It is clear from Figure 2b that, by controlling d_{TiO_2}, TP resonance can be tuned to occur at any wavelengths in the DBR forbidden band. However, λ_{TP} does not show a linear dependence on d_{TiO_2} due to the cavity and material dispersion. The interval between two neighboring TP resonances for a given wavelength λ is $\lambda/2n$ (refractive index n = 2.4 for TiO_2).[49] Figure 2d shows that λ_{TP} increases almost linearly with λ_{DBR}, which is consistent with the prediction when the Bragg frequency ($\hbar\omega_0$ = 1.65 eV) is much lower than the plasma frequency of gold ($\hbar\omega_p$ = 8.9 eV).[29,50] These observations show that the TP resonance can be tuned in a wide spectral range, which covers the visible or even the near-infrared bands for hot-electron photodetection.

The detailed optical response of the TP-HE PD is plotted in Figure 3a. It is shown that: 1) at the TP resonance, the reflection of the device is negligible (R ~ 1.6%); while for the off-resonance cases, nearly the entire incidence is reflected back by the highly reflective DBR; 2) over 87% of the light is absorbed preferentially by the top Au layer due to the excitation of TP at the MSM/DBR interface; 3) compared to the top Au layer, the bottom Au layer shows a much weak absorption (~10.6%), ensuring an asymmetrical optical absorption. For comparison, Figure S2a of the *Supporting Information* presents the results for the conventional grating-based SP-HE PD, in which the thicknesses of the top Au, ZnO, and the bottom Au layers are identical to those of the TP-HE PD shown in Figure 3a; in this case, the key parameters to determine the resonant wavelength are the period and width of the grating, which are identified to be 800 and 280 nm, respectively, in order to excite SP resonance at the same wavelength (813 nm). It indicates that the absorption in the top Au layer is only 37% by the excitation of SPs, much less than half of that by TP. Moreover, the absorption in the bottom Au layer is divided into two parts, but only the absorption (~6.2%) directly beneath the top stripe [*i.e.*, region 1 shown in the inset of Figure S2a contributes to the (counter-directional) photocurrent because the hot electrons generated in region 2 have a negligible probability to diffuse to the M/S interface.[13,15]

The initial hot electron energy distribution $D(E)$ can be written and normalized as: [14,51–53]

$$D(E) = \frac{\rho(E-h\upsilon)f(E-h\upsilon)\rho(E)[1-f(E)]}{\int \rho(E-h\upsilon)f(E-h\upsilon)\rho(E)[1-f(E)]dE} \quad (2)$$

where E is the energy of the excited electron, $h\nu$ the photon energy, $\rho(E-h\upsilon)$ [$\rho(E)$] the parabolic electron density of states at the initial [final] energy level, and $f(E-h\upsilon)$ [$f(E)$] the corresponding Fermi distribution function. Based on the assumption of an isotropic initial momentum distribution and using the exponential attenuation model, the probability that a hot electron reaches the M/S interface is evaluated by: [13,54,55]

$$P_1(x,z,E) = \frac{1}{2\pi}\int_{\theta_1}^{\theta_2} \exp\left(-\frac{d(x,z)}{\lambda_e(E)\,|\cos\theta|}\right)d\theta \qquad (3)$$

where d is the distance from the generation position of the hot electrons to the M/S interface, θ the moving angle of hot electrons, and λ_e the energy-dependent MFP of hot electrons accounting for electron–electron and electron-phonon contributions.[44] With the initial energy distribution $D(E)$ of hot electrons, the spatial distributions of the hot electron generation rate $G(x, z)$, and the energy-dependent transport probability $P_1(x, z, E)$, the flux of hot electrons reaching the top or the bottom M/S interface in the TP-based HE PDs can be written as:

$$N(x,z,E) = G(x,z) \times D(E) \times P_1(x,z,E) \qquad (4)$$

To compare extensively the internal photoemission efficiency of the hot-electron devices based on TPs and SPs, we take the electron with an excess energy (E_c) of 0.9 eV above the Fermi level as an example to depict the spatial distributions of the hot-electron generation rate as well as the probability and flux that the hot electrons reach the M/S interface before thermalization in Figures 3b–3d (in the main text) and Figures S2b–S2d (in the *Supporting Information*). It is found that: 1) for the TP-HE PD, the hot electrons are predominantly generated in the top Au layer, which leads to a strong hot-electron flow from the top Au layer to the bottom. For the SP-HE PD, most hot electrons are generated in the region close to the upper surface (or the corners) of the top (bottom) Au layer; 2) for the TP device, the probability for the hot electrons near the M/S interface is as large as 0.5 and decreases with the increase of the distance from the M/S interface towards both terminals. While for the grating system, not only the distance from the M/S interface but also the diffusion angle plays an important role. For example, P_1 in region 2 shown in the inset of Figure S2a is nearly zero as shown by Figure S2c. Accordingly, we can therefore see that some nanostructured systems might not take full use of the metal layers for hot-electron collection compared to the planar systems; 3) for the TP-based devices, due to the ultra-thin top Au layer with a thickness comparable to the MFP (~ 21 nm for E_c = 0.9 eV) of electrons in Au, the hot electrons generated in the entire top Au layer have a high chance to reach the interface without essential relaxation.[56] As a result, a large part of the hot electrons can participate in the interfacial electron transfer process and contribute to the detected photocurrent. Nevertheless, for the grating-based system, the flux of the hot electrons reaching the M/S interface is far less, as shown by Figure S2d.

The initial energy distribution of the hot electrons excited by the photons with wavelength of 813 nm is shown in Figure 4a, where the shaded area shows the proportion of hot electrons with energy above the Schottky barrier. After transportation, the final energy distributions of the hot electrons reaching the top and bottom M/S interfaces are provided in Figure 4b and Figure 4c, respectively. Following the model based on accessing the emission probability and multiple reflection losses as a result of an impedance mismatch of electrons between metal and semiconductor,[13,54] the probability for the hot electrons accumulated at the interface to be injected into the semiconductor [$P_2(E)$], propagate through the ultra-thin intermediate layer without being scattered [$P_3(E)$], and transmit through the opposite S/M interface [$P_4(E)$] can be calculated.[13] The net photocurrent density J_{Net} can be expressed as:

$$J_{\mathrm{Net}} = e(\iiint N_{\mathrm{top}\to\mathrm{bot}}(x,z,E) \times P_2(E)P_3(E)P_4(E)dxdzdE - \iiint N_{\mathrm{bot}\to\mathrm{top}}(x,z,E) \times P_2(E)P_3(E)P_4(E)dxdzdE \quad (5)$$

where $N_{\mathrm{top}\to\mathrm{bot}}$ ($N_{\mathrm{bot}\to\mathrm{top}}$) is the hot-electron flux reaching the top (bottom) M/S interface.

Figure 4d shows the calculated photoresponsivities of the TP- and grating-based SP-HE PDs as a function of the applied voltage (V_{app}) at the resonant wavelength. The result indicates that the unbiased photoresponsivity of the TP-HE PD is as high as 13.7 nA/mW, which is over 2 times larger than that of the grating-based system (6.5 nA/mW). The underlying physics can be explained as follows. In the conventional grating-based HE PDs, although strong plasmonic resonance can be excited, the incident light can directly interact with (and to be absorbed by) the bottom metal layer; however, in the TP systems, the incident light must interact with the top metal layer first with strong TP excitation so that the bottom metal absorption can be effectively suppressed. The strongly improved asymmetrical optical absorption in TP system ensures the strongly improved photoresponsivity. The photoresponsivities of both devices can be further enhanced by applying a forward electric bias (positive/negative contact connects the bottom/top Au electrode), which promotes the kinetic energy of the hot electrons in the semiconductor and results in a higher transmission probability as illustrated by the inset in the left-top corner of Figure 4d. The photoresponsivities of both HE PDs *versus* the barrier height are plotted in

Figure 4e, where the corresponding IQE curves of the TP-HE PD have been inserted. It is found that the responsivity can be decreased by an order of magnitude with Φ_B increasing from 0.4 to 1.2 eV,[27,51] which leads to decreased IQEs. In all positive biases and barrier situations, the photoresponsivities of the grating-based HE PD are lower than those of the TP system because these two systems show similar dependences on V_{app} and Φ_B, while the TP system exhibits much better optical performance.

As both the eigenfrequency of TPs and the extraction efficiency of hot electrons are sensitive to the metal thicknesses,[29,30] especially the thickness of the top Au layer d_{Au}, the effect of d_{Au} on the optical and electrical responses are examined in Figure 5. The dependence of the TP resonance on d_{Au} is shown in Figure 5a, where the corresponding TP resonant wavelengths are given by the inset. It is observed that a thick-enough top Au layer (over 50 nm) stabilizes the spectral position for TP excitation, verified by a very distinct band of reflection dips. The detailed optical components, *i.e.*, top Au absorption, bottom Au absorption, and device reflection are shown in Figure 5b. It is found that: 1) by using the DBR+MSM configuration, nearly all incident energy can be absorbed by the device under the TP mechanism and 2) a high net absorption requires a relatively thick top Au layer. However, the improved asymmetric optical absorption does not certainly lead to a high responsivity since the generated hot electrons in a thick Au layer suffer from the high thermalization losses by electron-electron and electron-phonon scatterings.[15,27] As a result, the optimal photoresponsivity occurs at $d_{Au} \sim 20$ nm.

We would like to indicate also that the highly sensitive photoresponsivity by TP-HE PD can be sustained simultaneously over a wide range of incident angle; moreover, the proposed TP-HE PD system can be extended to show rich functionalities, *e.g.*, multiband photodetection. The detailed discussions refer to Sections 4 and 5 of the *Supporting Information*.

Finally, we provide a detailed comparison with the existing measurements to show the validity of the modeling approach and the state-of-the-art hot-electron based photodetectors. It is noted that the predicted performance is not that high compared with some of the previous designs. However, the key difference lies in the various system configurations (based on different operation mechanisms) and operation wavelengths. For example, 1) the Schottky devices where highly doped semiconductor is used, the quantum efficiency of MIM is relatively low, primarily due to additional reflection losses arising from the additional MI interface;[12,15,57,58] 2) the significant photogain in bilayer MoS_2 with hot electron injection shows a much higher efficiency.[59] While if we compare MIM-based devices, the responsivity of the TP-HE PD is comparable to or even higher than that (9 nA/mW) of the plasmonically enhanced hot electron device.[60] In addition, compared to the references with Au/Al_2O_3 contact (Φ_B = 2.6 eV),[13,55] the responsivity in this study (*i.e.*, 13.7 nA/mW) has been significantly improved compared to the references (*i.e.*, responsivity < 80 nA/W) due to a much lower barrier is formed in Au/ZnO contact (Φ_B = 0.9 eV) in this study.

CONCLUSIONS

In summary, we present a purely planar setup for hot-electron photodetection without employing the conventional highly nanostructured components. The TP-HE PD is composed of a MSM hot-electron stack integrated with a front DBR. Such a hybrid system can excite a very strong TP resonance, which confines the incident photon energy in a region very close to the top Au layer, so that the highly asymmetric and strongly enhanced optical absorption can be realized to ensure a unidirectional hot-electron flow. In addition, the top Au layer and intermediate ZnO layer used are extremely thin to ensure a high efficiency of the internal photoemission process. We extensively investigate the tunability and optimization of the TP excitation in the DBR-MSM hybrid system by controlling the DBR pair number, DBR central wavelength, bottom DBR thickness, and top Au thickness. Results indicate that the system has a very high tunability with a very broad range (long to infrared region) for the TP resonance, a good tolerance to the change of incident angle, and the possibility to realize extended functionalities of hot-electron photodetection. An optimized TP-HE PD exhibits a photoresponsivity which can be over 2 times of the conventional grating-based HE PD. To conclude, the TP hot-electron strategy based on purely planar layers with even higher optoelectronic performance than the nanostructured equivalents shows a great potential for compact, highly sensitive, and low-cost applications in photodetection, bio-sensing, and imaging.

METHODS

Optoelectronic simulation of the TP-HE PD. Simulation is performed in this study with addressing both the electromagnetic and electrical responses of the TP-HE PD. The electromagnetic response is achieved by solving the Maxwell's equations *via* the finite-element method (FEM). The optical absorption, electrical field distribution, Tamm plasmon resonance, *etc.*, can all be investigated. In the electrical treatment, the carrier generation rate is obtained by directly converting the absorbed photons into the hot electrons. It further involves the calculation of the initial hot-electron energy distribution, the detailed hot-electron diffusion inside the metal layer, and the forthcoming hot-electron transportation processes through the MS interfaces and the semiconductor layer. The device photocurrent is obtained by calculating the downward and upward photocurrents based on the above optoelectronic simulation. A detailed description of the optoelectronic simulation method is provided in the *Supporting Information*.

ASSOCIATED CONTENT

Supporting Information

Optoelectronic model, more about Tamm plasmons, analysis of SP-HE PD photoemission process, angular performance of TP-HE PD and multiband hot-electron photodetection. This material is available free of charge *via* the Internet at http://acsnano.org.

Corresponding Author

*X. L. E-mail: xfli@suda.edu.cn

Author contributions

C.Z. carried out the design, organized the figures and drafted the manuscript. K.W. contributed to the preliminary calculations. X.L. conceived the design and supervised (together with V.G.) the research. C.Z., X.L., and V.G. contributed to the revision of the manuscript and Supporting Information. All authors read and approved the final manuscript.

Notes

The authors declare no competing financial interest.

ACKNOWLEDGEMENTS

This work is supported by National Natural Science Foundation of China (61675142), the Youth 973 Program (2015CB932700), Ph.D. Programs Foundation of Ministry of Education of China (20133201110021), Natural Science Foundation of Jiangsu Province of China (BK20141200), and Priority Academic Program Development (PAPD) of Jiangsu Higher Education Institutions.

REFERENCES

(1) Knight, M. W.; Sobhani, H.; Nordlander, P.; Halas, N. J. Photodetection with Active Optical Antennas. *Science* **2011**, *332*, 702–704.

(2) Mubeen, S.; Hernandez-Sosa, G.; Moses, D.; Lee, J.; Moskovits, M. Plasmonic Photosensitization of a Wide Band Gap Semiconductor: Converting Plasmons to Charge Carriers. *Nano Lett.* **2011**, *11*, 5548–5552.

(3) Lee, Y. K.; Jung, C. H.; Park, J.; Seo, H.; Somorjai, G. A; Park, J. Y. Surface Plasmon-Driven Hot Electron Flow Probed with Metal-Semiconductor Nanodiodes. *Nano Lett.* **2011**, *11*, 4251–4255.

(4) Wang, F.; Melosh, N. A. Power-Independent Wavelength Determination by Hot Carrier Collection in Metal-Insulator-Metal Devices. *Nat. Commun.* **2013**, *4*, 1711.

(5) Moskovits, M. Hot Electrons Cross Boundaries. *Science* **2011**, *332*, 676–677.

(6) Clavero, C. Plasmon-Induced Hot-Electron Generation at Nanoparticle/Metal-Oxide Interfaces for Photovoltaic and Photocatalytic Devices. *Nat. Photon.* **2014**, *8*, 95–103.

(7) Smith, J. G; Faucheaux, J. A.; Jain, P. K. Plasmon Resonances for Solar Energy Harvesting: A Mechanistic Outlook. *Nano Today* **2015**, *10*, 67–80.

(8) Li, J.; Cushing, S. K.; Zheng, P.; Meng, F.; Chu, D.; Wu, N. Plasmon-Induced Photonic and Energy-Transfer Enhancement of Solar Water Splitting by a Hematite Nanorod Array. *Nat. Commun.* **2013**, *4*, 2651.

(9) Mukherjee, S.; Libisch, F.; Large, N.; Neumann, O.; Brown, L. V.; Cheng, J.; Lassiter, J. B.; Carter, E. A.; Nordlander, P.; Halas, N. J. Hot Electrons do the Impossible: Plasmon-Induced Dissociation of H_2 on Au. *Nano Lett.* **2013**, *13*, 240–247.

(10) Schuck, P. J. Nanoimaging: Hot Electrons Go through the Barrier. *Nat. Nanotechnol.* **2013**, *8*, 799–800.

(11) Giugni, A.; Torre, B.; Toma, A.; Francardi, M.; Malerba, M.; Alabastri, A.; Zaccaria, R. P.; Stockman, M. I.; Fabrizio, E. D. Hot-Electron Nanoscopy Using Adiabatic Compression of Surface Plasmons. *Nat. Nanotechnol.* **2013**, *8*, 845–852.

(12) Sobhani, A.; Knight, M. W.; Wang, Y.; Zheng, B.; King, N. S.; Brown, L. V.; Fang, Z.; Nordlander, P.; Halas, N. J. Narrowband Photodetection in the Near-Infrared with a Plasmon-Induced Hot Electron Device. *Nat. Commun.* **2013**, *4*, 1643.

(13) Chalabi, H.; Schoen, D.; Brongersma, M. L. Hot-Electron Photodetection with a Plasmonic Nanostripe Antenna. *Nano Lett.* **2014**, *14*, 1374–1380.

(14) White, T. P.; Catchpole, K. R. Plasmon-Enhanced Internal Photoemission for Photovoltaics: Theoretical Efficiency Limits. *Appl. Phys. Lett.* **2012**, *101*, 073905.

(15) Zheng, B. Y.; Zhao, H.; Manjavacas, A.; McClain, M.; Nordlander, P. Distinguishing between Plasmon-Induced and Photoexcited Carriers in a Device Geometry. *Nat. Commun.* **2015**, *6*, 7797.

(16) Li, W.; Valentine, J. Metamaterial Perfect Absorber Based Hot Electron Photodetection. *Nano Lett.* **2014**, *14*, 3510–3514.

(17) Moskovits, M. The Case for Plasmon-Derived Hot Carrier Devices. *Nat. Nanotechnol.* **2015**, *10*, 6–8.

(18) Govorov, A. O.; Zhang, H.; Demir, H. V.; Gun'ko, Y. K. Photogeneration of Hot Plasmonic Electrons with Metal Nanocrystals: Quantum Description and Potential Applications. *Nano Today* **2014**, *9*, 85–101.

(19) Brongersma, M. L.; Halas, N. J.; Nordlander, P. Plasmon-Induced Hot Carrier Science and Technology. *Nat. Nanotechnol.* **2015**, *10*, 25–34.

(20) Sundararaman, R.; Narang, P.; Jermyn, A. S.; Goddard III, W. A.; Atwater, H. A. Theoretical Predictions for Hot-Carrier Generation from Surface Plasmon Decay. *Nat. Commun.* **2014**, *5*, 5788.

(21) Ueno, K; Misawa, H. Plasmon-Enhanced Photocurrent Generation and Water Oxidation from Visible to Near-Infrared Wavelengths. *NPG Asia Mater.* **2013**, *5*, e61.

(22) Knight, M. W.; Wang, Y.; Urban, A. S.; Sobhani, A.; Zheng, B. Y.; Nordlander, P.; Halas, N. J. Embedding Plasmonic Nanostructure Diodes Enhances Hot Electron Emission. *Nano Lett.* **2013**, *13*, 1687–1692.

(23) Lin, K.-T.; Chen, H.-L.; Lai, Y.-S.; Yu, C.-C. Silicon-Based Broadband Antenna for High Responsivity and Polarization-Insensitive Photodetection at Telecommunication Wavelengths. *Nat. Commun.* **2014**, *5*, 3288.

(24) Goykhman, I.; Desiatov, B.; Khurgin, J.; Shappir, J.; Levy, U. Locally Oxidized Silicon Surface-Plasmon Schottky Detector for Telecom Regime. *Nano Lett.* **2011**, *11*, 2219–2224.

(25) Wu, K.; Zhan, Y.; Zhang, C.; Wu, S.; Li, X. Strong and Highly Asymmetrical Optical Absorption in Conformal Metal-Semiconductor-Metal Grating System for Plasmonic Hot-Electron Photodetection Application. *Sci. Rep.* **2015**, *5*, 14304.

(26) Fang, Y.; Jiao, Y.; Xiong, K.; Ogier, R.; Yang, Z. J; Gao, S.; Dahlin, A. B.; Käll, M. Plasmon Enhanced Internal Photoemission in Antenna-Spacer-Mirror Based Au/TiO_2 Nanostructures. *Nano Lett.* **2015**, *15*, 4059–4065.

(27) Wang, F.; Melosh, N. A. Plasmonic Energy Collection through Hot Carrier Extraction. *Nano Lett.* **2011**, *11*, 5426–5430.

(28) Zhang, C.; Wu, K.; Zhan, Y.; Giannini, V.; Li, X. Planar Microcavity-Integrated Hot-Electron Photodetector. *Nanoscale* **2016**, *8*, 10323–10329.

(29) Kaliteevski, M.; Iorsh, I.; Brand, S.; Abram, R. A.; Chamberlain, J. M, Kavokin, A. V.; Shelykh, I. A. Tamm Plasmon-Polaritons: Possible Electromagnetic States at the Interface of a Metal and a Dielectric Bragg Mirror. *Phys. Rev. B* **2007**, *76*, 165415.

(30) Sasin, M. E.; Seisyan, R. P.; Kalitteevski, M. A.; Brand, S.; Abram, R. A; Chamberlain, J. M.; Egorov, A. Yu.; Vasil'ev, A. P.; Mikhrin, V. S.; Kavokin, A. V. Tamm Plasmon Polaritons: Slow and Spatially Compact Light. *Appl. Phys. Lett.* **2008**, *92*, 251112.

(31) Grossmann, C.; Coulson, C.; Christmann, G.; Farrer, I.; Beere, H. E.; Ritchie, D. A.; Baumberg, J. J. Tuneable Polaritonics at Room Temperature with Strongly Coupled Tamm Plasmon Polaritons in Metal/Air-Gap Microcavities. *Appl. Phys. Lett.* **2011**, *98*, 231105.

(32) Chen, Y.; Zhang, D.; Qiu, D.; Zhu, L.; Yu, S.; Yao, P.; Wang, P.; Ming, H.; Badugu, R.; Lakowicz, J. R. Back Focal Plane Imaging of Tamm Plasmons and Their Coupled Emission. *Laser Photon. Rev.* **2014**, *8*, 933–940.

(33) Zhang, X. F. Song, J. F.; Li, X. B.; Feng, J.; Sun, H. B. Optical Tamm States Enhanced Broad-Band Absorption of Organic Solar Cells. *Appl. Phys. Lett.* **2012**, *101*, 243901.

(34) Zhang, X. L.; Song, J. F.; Feng, J.; Sun, H. B. Spectral Engineering by Flexible Tunings of Optical Tamm States and Fabry–Perot Cavity Resonance. *Opt. Lett.* **2013**, *38*, 4382–4385.

(35) Zhang, W. L.; Wang, F.; Rao, Y. J.; Jiang, Y. Novel Sensing Concept Based on Optical Tamm Plasmon. *Opt. Express* **2014**, *22*, 14524–14529.

(36) Das, R.; Srivastava, T.; Jha, R. Tamm-Plasmon and Surface-Plasmon Hybrid-Mode Based Refractometry in Photonic Bandgap Structures. *Opt. Lett.* **2014**, *39*, 896–899.

(37) Auguié, B.; Fuertes, M. C.; Angelomé, P. C.; Abdala, N. L.; Soler Illia, G. J.; Fainstein, A. Tamm Plasmon Resonance in Mesoporous Multilayers: toward a Sensing Application. *ACS Photonics* 2014, *1*, 775–780.

(38) Kavokin, A.; Shelykh, I.; Malpuech, G. Optical Tamm States for the Fabrication of Polariton Lasers. *Appl. Phys. Lett.* **2005**, *87*, 261105.

(39) Azzini, S.; Lheureux, G.; Symonds, C.; Benoit, J. M.; Senellart, P.; Lemaitre, A.; Greffet, A.; Blanchard, C.; Sauvan, C.; Bellessa, J. Generation and Spatial Control of Hybrid Tamm Plasmon/Surface Plasmon Modes. *ACS Photonics* **2016**, *3*, 1776–1781.

(40) Liew, T. C. H.; Kavokin, A. V.; Shelykh, I. A. Optical Circuits Based on Polariton Neurons in Semiconductor Microcavities. *Phys. Rev. Lett.* **2008**, *101*, 016402.

(41) Srikant, V.; Clarke, D. R. On the Optical Band Gap of Zinc Oxide. *J. Appl. Phys.* **1998**, *83*, 5447–5451.

(42) Kasap, S. O. Principles of Electronic Materials and Devices, 2006.

(43) Jacobi, K.; Zwicker, G.; Gutmann, A. Work Function, Electron Affinity and Band Bending of Zinc Oxide Surfaces. *Surf. Sci.* **1984**, *141*, 109–125.

(44) Brown, A. M.; Sundararaman, R.; Narang, P.; Goddard III, W. A.; Atwater, H. A. Nonradiative Plasmon Decay and Hot Carrier Dynamics: Effects of Phonons, Surfaces, and Geometry. *ACS Nano* **2015**, *10*, 957–966.

(45) Palik, E. D. Handbook of Optical Constants of Solids, Academic Press, Orlando, 1985.

(46) Moharam, M. G.; Grann, E. B.; Pommet, D A.; Gaylord, T. K. Formulation for Stable and Efficient Implementation of the Rigorous Coupled-Wave Analysis of Binary Gratings. *J. Opt. Soc. Am. A* **1995**, *12*, 1068–1076.

(47) Comsol Multiphysics, Available from: http://www.comsol.com/; Accessed Jan 9, 2017.

(48) Li, X.; Zhan, Y. Enhanced External Quantum Efficiency in Rectangular Single Nanowire Solar Cells. *Appl. Phys. Lett.* **2013**, *102*, 021101.

(49) Zhou, H.; Yang, G.; Wang, K.; Long, H.; Lu, P. Multiple Optical Tamm States at a Metal–Dielectric Mirror Interface. *Opt. Lett.* **2010**, *35*, 4112–4114.

(50) Zeman, E. J.; Schatz, G. C. An Accurate Electromagnetic Theory Study of Surface Enhancement Factors for Silver, Gold, Copper, Lithium, Sodium, Aluminum, Gallium, Indium, Zinc, and Cadmium. *J. Phys. Chem.* **1987**, *91*, 634–643.

(51) Ng, C.; Cadusch, J. J.; Dligatch, S.; Roberts, A.; Davis, T. J.; Mulvaney, P.; Gómez, D. E. Hot Carrier Extraction with Plasmonic Broadband Absorbers. *ACS Nano* **2016**, *10*, 4704–4711.

(52) Gong, T.; Munday, J. N. Materials for Hot Carrier Plasmonics. *Opt. Mater. Express* 2015, *5*, 2501–2512.

(53) Narang, P.; Sundararaman, R.; Atwater, H. A. Plasmonic Hot Carrier Dynamics in Solid-State and Chemical Systems for Energy Conversion. *Nanophotonics* **2016**, *5*, 96–111.

(54) Scales, C.; Berini, P. Thin-Film Schottky Barrier Photodetector Models. *IEEE J. Quantum Electron.* **2010**, *46*, 633–643.

(55) Gong, T.; Munday, J. N. Angle-Independent Hot Carrier Generation and Collection Using Transparent Conducting Oxides. *Nano. Lett.* **2014**, *15*, 147–152.

(56) Zhang, C.; Wu, K.; Ling, B.; Li, X. Conformal TCO-Semiconductor-Metal Nanowire Array for Narrowband and Polarization-Insensitive Hot-Electron Photodetection Application. *J. Photon. Energy* **2016**, *6*, 042502.

(57) Li, W.; Valentine, J. G. Harvesting the Loss: Surface Plasmon-Based Hot Electron Photodetection. *Nanophotonics* **2017**, *6*, 177–191.

(58) Sharma, A.; Kumar, R.; Bhattacharyya, B.; Husale, S. Hot Electron Induced NIR Detection in CdS Films. *Sci. Rep.* **2016**, *6*, 22939.

(59) Wang, W.; Klots, A.; Prasai, D.; Yang, Y.; Bolotin, K. I.; Valentine, J. Hot Electron-Based Near-Infrared Photodetection Using Bilayer MoS_2. *Nano Lett.* **2015**, *15*, 7440–7444.

(60) Atar, F. B.; Battal, E.; Aygun, L. E.; Daglar, B.; Bayindir, M.; Okyay, A. K. Plasmonically Enhanced Hot Electron Based Photovoltaic Device. Opt. Express **2013**, *21*, 7196–7201.

Figures and captions

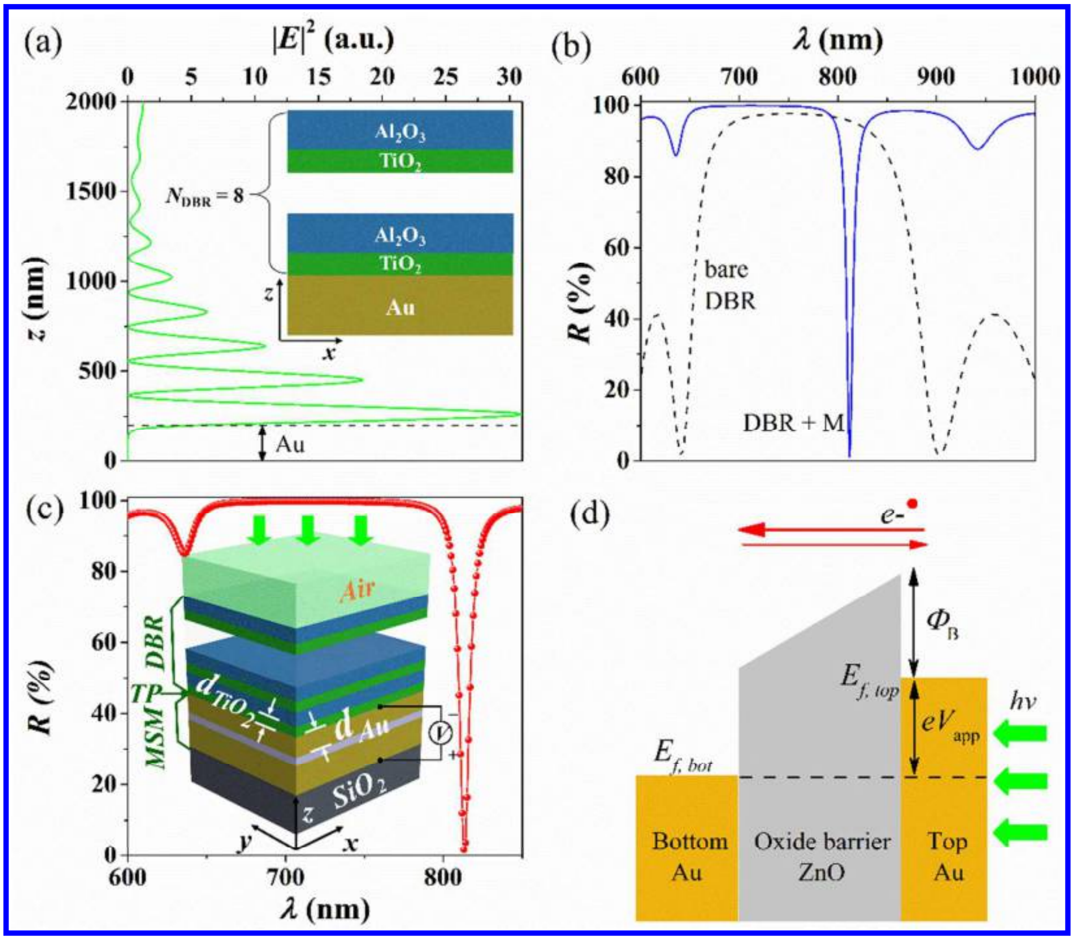

Figure 1. (a) The profile of the normalized electric field $|E|^2$ along z axis for a TP at the interface between a front 8-pair DBR and a semi-infinite Au layer. The schematic of the classic Tamm structure (DBR + M) is shown in the inset. (b) Reflection spectra $R(\lambda)$ of the bare DBR and DBR + M structures. (c) Reflection spectra $R(\lambda)$ of the TP-based hot-electron photodetector (TP-HE PD) with the corresponding schematic diagram inserted. (d) Energy band diagram of the TP-HE PD. Unless specific indication, the thicknesses of the top Au, intermediate ZnO, and bottom Au layers are 25, 5, and 200 nm, respectively; the DBR consists of 8 pairs (DBR pair number N_{DBR} = 8) of alternating Al_2O_3/TiO_2 layers (each layer with quarter-wavelength optical thickness, where the DBR central wavelength λ_{DBR} is initially considered to be 750 nm). The thicknesses of the bottom TiO_2 layer and top Au layer are defined as d_{TiO_2} and d_{Au}, respectively.

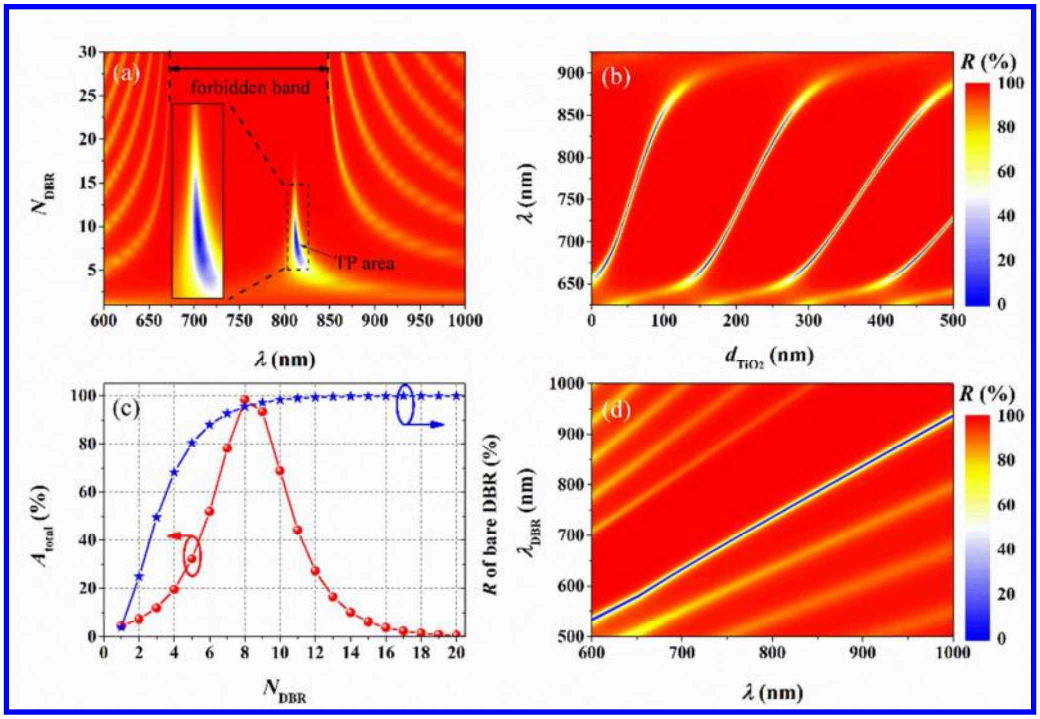

Figure 2. Dependences of the device reflection $R(\lambda)$ on (a) the DBR pair number N_{DBR}, (b) the bottom TiO_2 thickness d_{TiO_2} in DBR, and (d) the DBR central wavelength λ_{DBR}. Absorption and reflection of the entire TP-HE PD at TP wavelength λ_{TP} = 813 nm *versus* N_{DBR} are shown in (c). An enlarged figure showing the TP area is inserted in (a). The rest parameters are the same as those indicated in the caption of Figure 1.

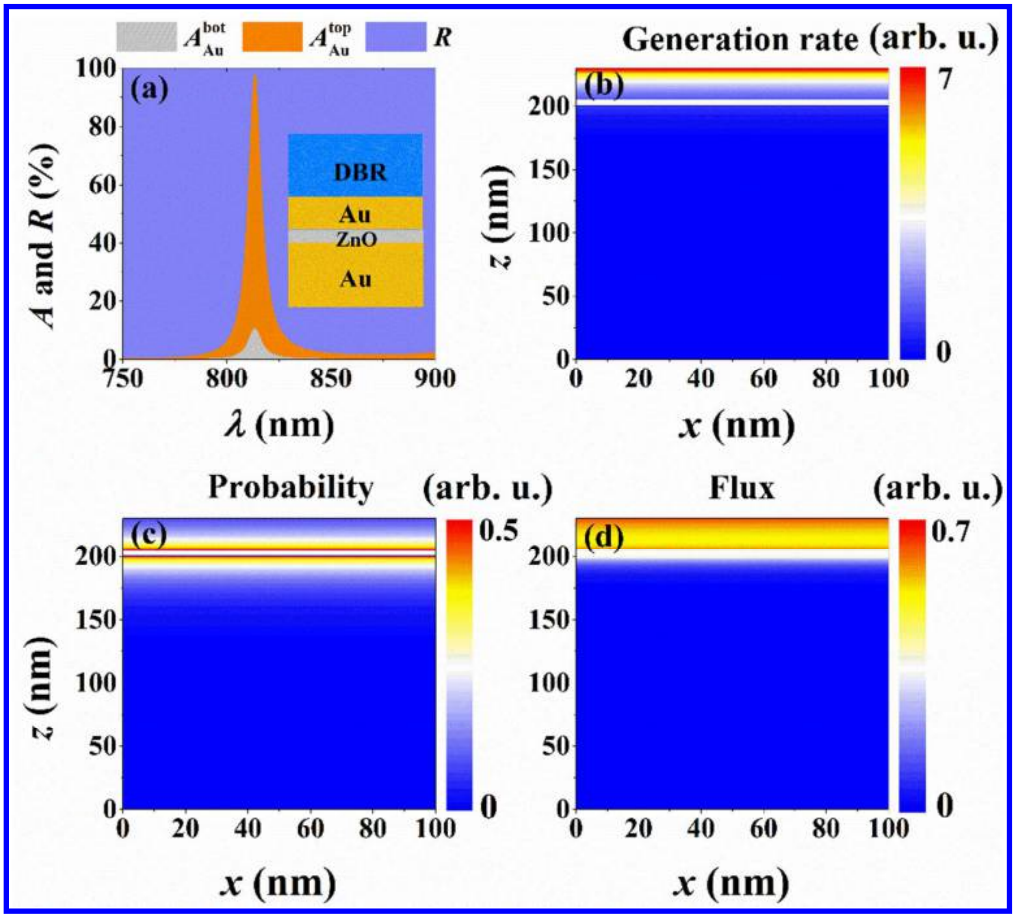

Figure 3. (a) the detailed optical responses; the spatial distributions of (b) the hot-electron generation rate, (c) the transport probability, and (d) the flux of hot electrons reaching the M/S interface before thermalization for excess energy of 0.9 eV. The device configuration of the TP-HE PD is inserted in (a). The device parameters used here are the same as those indicated in the caption of Figure 1.

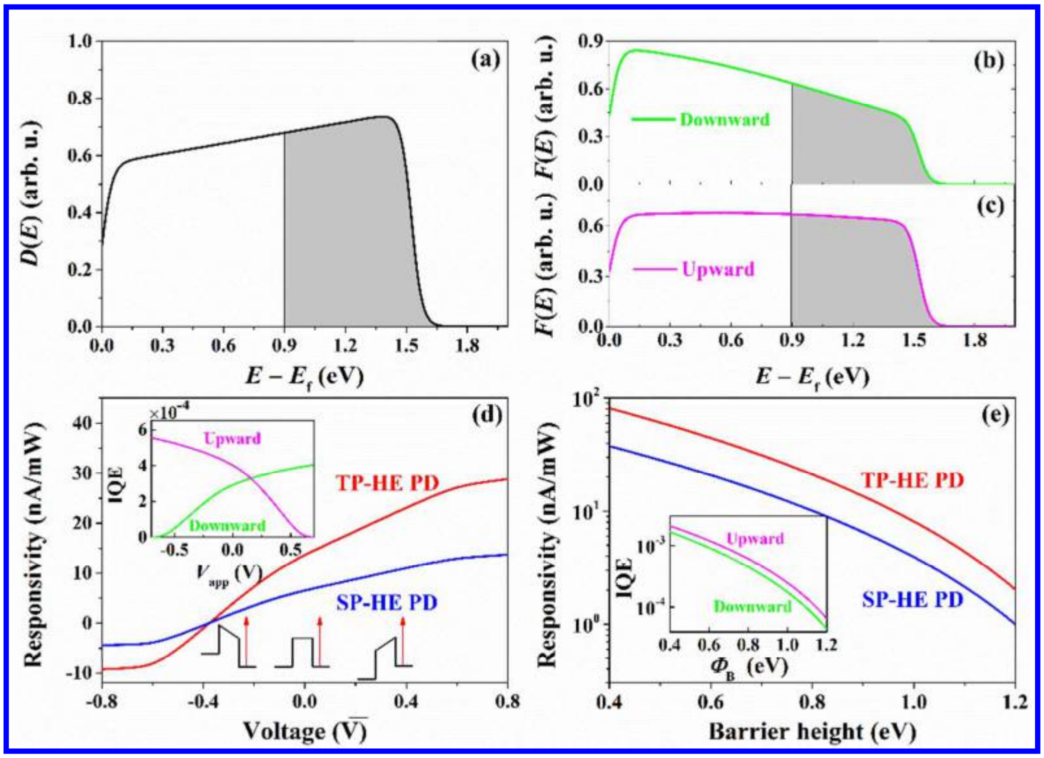

Figure 4. (a) The initial energy distribution of hot electron excited in Au by incident photons with wavelength of 813 nm. The horizontal scale represents the excess electron energy with respect to Fermi energy, E_f. The final distribution of hot electron energies accumulated at the top (b) and bottom (c) M/S interfaces considering the energy-dependent MFP. The responsivities of the TP- and SP-HE PDs as a function of (d) the electric bias V_{app} and (e) the barrier height Φ_B, where the device parameters are from Figure 1. The bottom (top) insets in Figure 4d are the energy band diagrams at reverse/zero/forward bias (the corresponding IQE *versus* the bias). The inset in Figure 4e are IQE *versus* the barrier height.

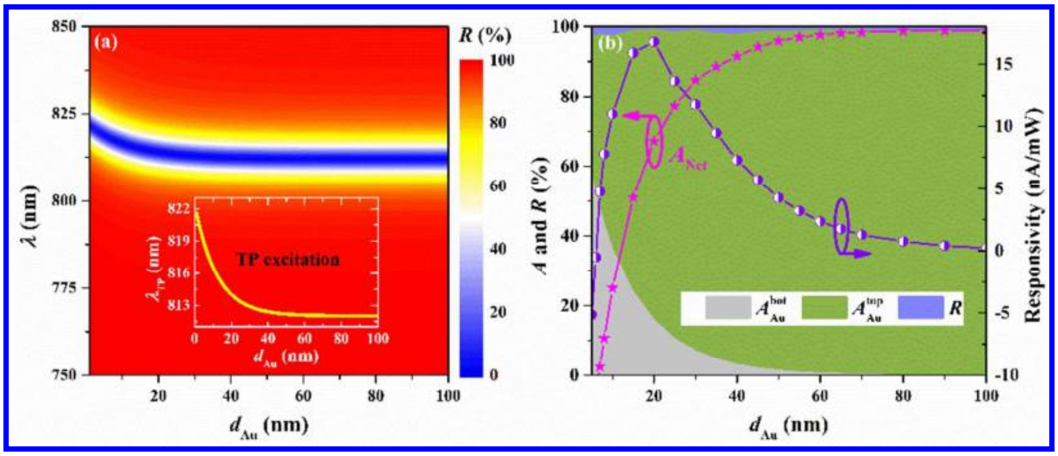

Figure 5. (a) Dependence of the device reflection spectrum $R(\lambda)$ on the top Au thickness d_{Au}, where the inset is the TP wavelength λ_{TP} *versus* d_{Au}. (b) The optical response and responsivity at the TP wavelength as a function of d_{Au}. The rest parameters are the same as those indicated in the caption of Figure 1.

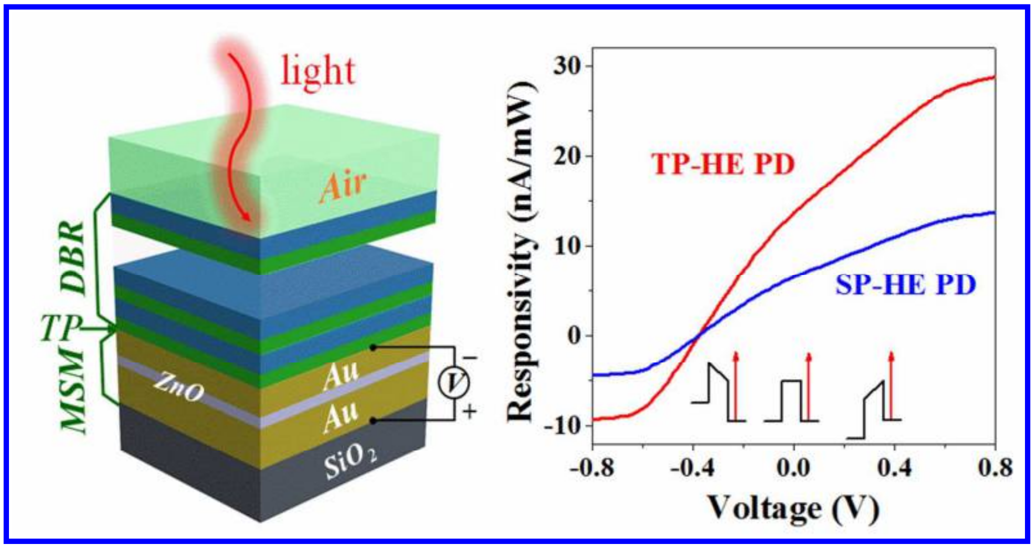

Table of Contents

80×41.5 mm (300×300 DPI)